

Observation of internal oxidation in a 20% cold-worked Fe-17Cr-12Ni stainless steel through high-resolution characterization

Zhao Shen^{1*}, David Tweddle¹, Mark Thomas Lapington¹, Benjamin Jenkins¹, Donghai Du², Lefu Zhang², Michael P. Moody¹, Sergio Lozano-Perez²

¹Department of Materials, University of Oxford, Parks Road, OX1 3PH Oxford, UK

²School of Nuclear Science and Engineering, Shanghai Jiao Tong University, 800 Dongchuan Road, Shanghai 200240, China

*Corresponding author: zhao.shen@materials.ox.ac.uk

Abstract: It is often assumed that internal oxidation cannot occur at temperatures below 400°C. However, in the present work, internal oxidation was observed in a 20% cold-worked Fe-17Cr-12Ni stainless steel (SS) after exposure to simulated primary water of a pressurized water reactor at 340°C and not in a similarly tested sample without prior cold-work. The formation of discrete Cr-oxide precipitates and the role of cold-work are discussed. The internal oxidation model is also proposed as a plausible stress corrosion cracking mechanism of Fe-17Cr-12Ni SS at that temperature.

Keywords: Stainless steel; Oxidation; Stress corrosion cracking; Transmission electron microscopy; Atom Probe Tomography.

Intergranular stress corrosion cracking (IGSCC) has affected structural materials exposed to primary water of pressurized water reactors (PWRs) [1-4]. To date, several mechanisms have been proposed that describe the mechanisms controlling IGSCC of austenitic alloys, including the slip-oxidation model [5], the hydrogen embrittlement model [6], the creep-cavity model [7], and the internal oxidation model (IOM) [8-11]. The IOM was firstly proposed by Scott et al. [8] in the study of IGSCC of Alloy 600 after exposure to the primary water of PWR. Criticisms to the IOM also exist due to the lack of experimental evidence of isolated selective oxidation ahead of the continuous oxide at such temperatures [12]. With recent advances on characterization techniques, several results have been reported confirming that internal oxidation can occur at temperatures below 400°C in Ni-based alloys [11, 13]. As a result, the IOM is gaining some momentum as a plausible IGSCC mechanism for Alloy 600.

Austenitic 316 stainless steel (SS) has been widely used in PWRs as structural components due to its combination of good mechanical properties and high general corrosion resistance [4, 14-19]. However, it also suffers from IGSCC [4, 14-19]. However, the IOM has generally not been considered as a plausible IGSCC mechanism for austenitic SS. In 2012, atom probe tomography (APT) was used by Kruska et al. [20] to study the chemical composition of the oxidized grain boundaries of 304 SS with prior 20% cold work after exposure to simulated PWR primary water for 1500h at 360°C. The authors observed the distribution of discrete Cr-rich oxide precipitates in one of the oxidized grain boundaries. Due to the lack of awareness of the importance of this observation, the formation of discrete oxide precipitates in the oxidized grain boundary was not fully investigated by these authors. However, this observation might be an evidence to support the existence of internal oxidation in the austenitic SS after exposure to the simulated PWR primary water environment.

It is generally believed that the internal oxidation cannot occur at the PWR operating temperature due to the low lattice diffusion of oxygen in the metal matrix at the relatively low-temperature environment (lower than 400°C) [21, 22]. This is the reason why the IOM was criticized by many researchers at the

early stage. However, the extra deformation introduced by the cold-work increases the number of vacancies and dislocations, especially at/around the grain boundaries, where the dislocations preferentially accumulate [11, 23]. Since cold-work in the structural materials used in the PWR primary water is inevitable during the component manufacture and installation, high content of defects can be expected in the materials. Once the defects exist, the inward diffusion of oxygen and the outer diffusion of cations can be accelerated, enabling internal oxidation at lower temperatures.

In the current study, high-resolution analytical transmission electron microscopy (TEM) and APT have been applied in the examination of internal oxidation in the 316 SS with and without cold-work after exposure to simulated PWR primary water for 2000h at 340°C. With the high-resolution observations obtained from the direct comparative study, the IOM is proposed as a plausible IGSCC mechanism for austenitic SS in the simulated PWR primary water environment.

The material used in this work was solution-annealed 316 SS, with a chemical composition of 17.28 Cr, 12.05 Ni, 2.48 Mo, 1.81 Mn, 0.43 Si, 0.014 C, 0.012 P, 0.001 S, and balance Fe (wt. %). The average grain size was ~100 μm . Cold work was introduced via cold rolling with a reduction of thickness of 20%. A pre-cracked 0.5T CT specimen was made from the 20% cold-worked 316 SS in the S-L orientation (according to ASTM E399) for IGSCC test. Two coupons with mirror-finished surfaces were prepared from 316 SS with and without cold-work for general corrosion test. The IGSCC and general corrosion tests were conducted in simulated PWR primary water at 340°C (hydrogenated water: 500 ppm B + 2 ppm Li + 30 cc/kg dissolved H_2). Although the PWR primary circuit operating temperature is 290-325°C, 340°C is chosen to accelerate the general corrosion and IGSCC without altering the operating mechanisms [20]. The two coupons were exposure for 2000 h. The CT specimen was tested under a constant load of 30 $\text{MPa}\cdot\text{m}^{1/2}$ and the crack growth rate was measured to be $\sim 6.21 \times 10^{-8}$ mm/s. Since the content of dissolved hydrogen located around the equilibrium of Ni/NiO, the formation of NiO is difficult [24].

A dual beam Zeiss Nvision 40 FIB-SEM was used to prepare TEM foils containing surface oxides and crack tips after the general corrosion and IGSCC tests, respectively. More details about the sample preparation can be found in [25]. High angle annular dark field (HAADF) imaging and electron energy loss spectroscopy (EELS) were conducted with a JEOL ARM 200F to reveal the morphology and chemical composition of the TEM foils. In addition, the curve fitting method in Hyperspy [26] which models the experimental spectra as a linear combination of an inverse power law (background) and all the relevant Hartree-Slater theoretical edges (O K and Cr, Fe, and Ni L), prior convolution with the low-loss spectra, was used to extract elemental maps. For the characterization of oxidation state, two extra Gaussians, accounting for the L_3 and L_2 peaks in the Cr, Fe and Ni L edges, were added to the model. More details can be found in [4, 27, 28].

APT samples were prepared by a dual beam Zeiss NVision 40 FIB-SEM. More details can be found in [20]. APT analysis was performed using a LEAP 5000 XR, with a detection efficiency of 52%. Samples were analysed using a laser energy (UV – 355 nm laser) of 45 pJ, sample temperature of 40 K, a pulse frequency of 200 kHz and a detection rate of 0.2%. The APT data was processed using IVAS 3.8.2, with the needle shape estimated using a voltage reconstruction.

Fig. 1a shows the cross-sectional morphology of the 20% cold-worked 316 SS after exposure to the simulated PWR primary water for 2000h at 340°C. A dual-layered surface oxide film is observed: an inner oxide layer (IOL) and an outer oxide layer (OOL). Similar results have been reported by many researchers [17, 29-31]. Further observation reveals the existence of a large number of oxide precipitates in the region beyond the IOL-metal matrix interface. The depth (or thickness) of this region

is ~100 nm. EELS mapping was conducted to show the chemical composition around the IOL-metal matrix. Fig. 1b shows the signal intensity maps of the major components, in which the brighter contrast indicates a greater net count. The IOL is enriched in Cr and depleted in Ni and Fe (compared to the metal matrix), which has been reported to consist of FeCr_2O_4 [4, 17]. The oxide precipitates in the region beyond the IOL-metal matrix interface are also enriched in Cr and depleted in Fe. Further observation reveals that these Cr-rich oxide precipitates are surrounded by Ni-rich circles. These Ni-rich regions are free of oxygen, suggesting that Ni in these regions exists in its metallic phase. The Ni-rich features were also reported by Langalier et al. [32] and Bertali et al. [33] in the study of internal oxidation of Alloy 600 in hydrogenated steam at 480°C. The authors attributed the formation of Ni-rich features to the expulsion of metallic Ni during the selective oxidation more reactive elements (such as Cr and/or Fe) under the low oxidation potential environment.

Internal oxidation is the process in which oxygen dissolves in a metal and diffuses inwards, reacting with the less-noble solute to form dispersed metal oxide precipitates [34]. As a result, to confirm the existence of internal oxidation, two distinguished features should be observed: one is the selective oxidation of the most reactive elements and the other one is the formation of discrete oxide precipitates (not directly connected to the IOL). Although the EELS chemical composition analysis provides a chemical composition for the oxide precipitates, due to the thickness-overlap issue between 5-10 at.% of Fe and Ni are also detected, suggesting that there is a contribution from the surrounding matrix over the thickness of the sample. Hence, simple quantitative analysis alone cannot prove the existence of selective oxidation.

To reveal the existence of selective oxidation, EELS oxidation state mapping was conducted. The location of the centre of the L_3 white lines is plotted for Cr and Fe in Figs. 1c and 1d, respectively. The higher the intensity of these images, the higher the oxidation state. As reported in [4], Cr only oxidizes to Cr^{3+} and Fe can oxidize to Fe^{2+} or Fe^{3+} . The results in Fig 1c show that Cr in the IOL and in the oxide precipitates is oxidized. The IOL was identified as FeCr_2O_4 by diffraction. However, Fig 1d shows that Fe in the IOL has been oxidized (mostly to Fe^{2+} although there are traces of Fe^{3+} in the upper region of the IOL), while it remains metallic in most of the regions with oxide precipitates. Since only Cr is oxidized in the oxide precipitates, and the local Cr content is higher than the matrix (Fig 1b), it is plausible to suggest that Cr_2O_3 is the main phase in these isolated precipitates. Low Ni content in the matrix results in poor statistics in the Ni L edge region, which have prevented the determination of the oxidation state of Ni in this work. However, since metallic Ni is thermodynamically more stable than metallic Fe at the PWR operating temperature [24, 35], Ni is assumed to exist in metallic state in the regions where Fe remains metallic. As a result, the selective oxidation of Cr in the oxide precipitates has been confirmed.

A careful examination of Fig 1d reveals that Fe has oxidized to Fe^{2+} in a part of the oxide precipitates (outlined by yellow dashed lines). These oxide precipitates appear to be connected to each other, forming an oxide channel which seems connected to the IOL. It is suggested that oxygen/water availability through the channel has resulted in enhanced oxygen diffusion along it, increasing the oxidation potential locally and enabling the local formation of FeCr_2O_4 .

Although the oxide precipitates are discretely distributed according to the TEM analysis, they may still be connected in three dimensions (3D) since TEM only displays the 2-dimensional projection of a thin foil. To prove that they are discrete in 3D, a 3D characterization technique is required. Consequently, APT was used to analyse the region containing the oxide precipitates. Fig. 3a shows a needle prepared from the region around the IOL-metal matrix interface. APT analysis shows that the IOL is enriched

in Cr and depleted in Fe and Ni, with a composition compatible with FeCr_2O_4 . The APT reconstructions reveal discrete Cr-rich precipitates. To show the 3D distribution of the oxide precipitates, 4.5 at.% O isosurfaces were reconstructed. The results confirm that the oxide precipitates are discrete in 3D and not connected to the IOL. A slice containing oxide precipitates has been extracted from the data set to show their composition. Fig. 2b shows that the oxide precipitates are enriched in Cr, depleted in Fe and appear to be surrounded by Ni-rich shells, which is similar to the Ni expulsion observed in Fig. 1b. Proximity histograms (proxigrams) can show the 1D concentration profiles of elements normal to the interface with the oxide precipitates. Several oxide precipitates in Fig. 2a (4.5 at.% O isosurfaces) are selected to show the 1D chemical composition across the interfaces, as shown in Fig. 2c. Although the proxigrams may not show the accurate chemical composition due to the evaporation artefacts that can arise during the field evaporation of secondary phases, we can still observe that Ni is enriched around the Cr-rich precipitates. As a result, the APT analysis also shows that Ni and Fe have been expelled during the selective oxidation of Cr. While Fe diffuses out to be oxidized in contact with the environment, Ni stays locally in metallic form. Together with the results shown in Fig. 1, we have demonstrated that Cr has been selectively oxidized and formed discrete oxide precipitates in 3D. Hence, it is sensible to conclude that internal oxidation has occurred in 316 SS with 20% cold-work at 340°C.

Fig. 3a shows the morphology around the IOL-metal matrix interface of the 316SS without cold-work after exposure to the simulated PWR primary water for 2000h at 340°C. Compared with the one with 20% cold-work (see Fig. 1a), no oxide precipitates are observed. EELS mapping shows that the chemical composition is uniform in the metal matrix and no Cr-rich precipitates are observed (see Fig. 3b). As a result, internal oxidation has not occurred in 316 SS without cold-work.

Since internal oxidation in 316 SS was only observed on samples with prior 20% cold-work, it is sensible to assume that cold-work plays an important role. Cold-work introduces extra defects such as vacancies or dislocations in the material. These defects can then act as fast-diffusion channels to accelerate the inward diffusion of oxygen and the outer diffusion of cations that are not selectively oxidized.

As reported in our prior work [15], the cold-work will lead to preferential deformation and higher defect density around grain boundaries. We can then consider if internal oxidation might also occur along intergranular cracks. Fig. 4a shows an IGSCC crack tip prepared from 316 SS tested in simulated PWR primary water at 340°C. The EELS mapping shows the existence of Cr-rich oxide precipitates (which appear discrete at places) in the grain boundary ahead of the IGSCC crack tip. In addition, discrete oxide precipitates were also observed in the SCC crack flanks (see Fig. 4b). The examined region in Fig. 4b is around 2 μm away from the IGSCC crack tip. Although the 3D characteristics of these oxide precipitates have not been examined by APT due to the difficulties in sample preparation, the morphology and chemical composition are very similar to that observed in the surface oxide of 20% cold-worked 316 SS. If we assume that cold-working has facilitated internal oxidation ahead of the crack tip, we can consider the IOM as a plausible IGSCC mechanism for 316 SS at 340°C. In any case, at this time, since the 3D characteristics of the oxide precipitates ahead of the IGSCC crack tip are still not clear, this is only speculation until further APT characterization of these region is achieved.

In summary, the combination of analytical TEM and 3D APT have proven the existence of selective and internal oxidation in a 20% cold-worked 316 SS after exposure to simulated PWR primary water at 340°C. The occurrence of internal oxidation requires prior cold working, which enables faster inward and outward lattice diffusion than otherwise possible at this temperature. Given the similarities of these

observations with those at the IGSCC crack tip region, the IOM is proposed as one of the operating IGSCC mechanisms. It is worth noting that irradiation can also introduce defects into the materials serviced in the PWR primary circuit. The potential effects of irradiation on the internal oxidation has not been addressed in the present study and will be the next step of our study.

Acknowledgments

The authors would like to thank the National Nature Science Foundation of China (No. 51871153) and the EPSRC (EP/K040375/1, EP/N010868/1 and EP/R009392/1) grants for funding this research. Zhao Shen is grateful to China Scholarship Council (CSC) for providing PhD studentship.

References

- [1] N. Totsuka, Z. Szklarska-Smialowska, *Corrosion* 44(1988) 124-126.
- [2] Y. Z. Huang, J. M. Titchmarsh, *Acta Mater.* 54(2006) 635-641.
- [3] S.M. Bruemmer, *Mater. Sci. Forum* 294(1999) 75-82.
- [4] Z. Shen, D. Du, L. Zhang, S. Lozano-Perez, *Corros. Sci.* 148(2019) 213-227.
- [5] F.P. Ford, *Corrosion* 52(1996) 375-395.
- [6] H.K. Birnbaum, P. Sofronis, *Mater. Sci. Eng. A* 176(1994) 191-202.
- [7] K. Arioka, T. Yamada, T. Terachi, T. Miyamoto, *Corrosion* 64(2008) 691-706.
- [8] P.M. Scott, M. Le Calver, in *Proceedings of the 6th International Symposium on Environmental Degradation of Materials in Nuclear Power Systems-Water Reactors* (1993), pp. 657-665.
- [9] B. Langelier, S. Y. Persaud, A. Korinek, T. Casagrande, R. C. Newman, G. A. Botton. *Acta Mater.* 131(2017) 280-295.
- [10] M.G. Burke, G. Bertali, E. Prestat, F. Scenini, S.J. Haigh, *Ultramicroscopy* 176(2017) 46-51.
- [11] Z. Shen, K. Chen, D. Tweddle, G. He, K. Arioka, S. Lozano-Perez, *Corros. Sci.* 152(2019) 82-92.
- [12] R.B. Rebak, Z. Szklarska-Smialowska: *Corros. Sci.* 38(1996) 971-88.
- [13] W. Kuang, M. Song, G.S. Was, *Acta Mater.* 151(2018) 321-333.
- [14] P. L. Andresen, C. L. Briant, *Corrosion* 45(1989) 448-463.
- [15] Z. Shen, M. Meisnar, K. Arioka, S. Lozano-Perez, *Acta Mater.* 165(2019) 73-86.
- [16] A. Turnbull, K. Mingard, J. D. Lord, B. Roebuck, D. R. Tice, K. J. Mottershead, N. D. Fairweather, A. K. Bradbury, *Corros. Sci.* 53(2011) 3398-3415.
- [17] T. Terachi, K. Fujii, K. Arioka, *J. Nucl. Sci. Technol.* 42(2005) 225-232.
- [18] R.P. Matthews, R.D. Knusten, J.E. Westraadt, T. Couvant, *Corros. Sci.* 125(2017) 175-183.
- [19] T. Liu, S. Xia, Q. Bai, B. Zhou, L. Zhang, Y. Lu, T. Shoji, *J. Nucl. Mater.* 498(2018) 290-299.
- [20] K. Kruska, S. Lozano-Perez, D.W. Saxey, T. Terachi, T. Yamada, G.D. Smith, *Corros. Sci.* 63(2012) 225-233.
- [21] R.A. Rapp, *Corrosion*, 21(1965) 382-401.

- [22] D. L. Douglass, *Oxid. Met.* 44(1995) 81-111.
- [23] K. Arioka, Y. Iijima, T. Miyamoto, *Int. J. Mater. Res.* 108(2017) 791-797.
- [24] P.L. Andresen, J. Hickling, A. Ahluwalia, J. Wilson, *Corrosion* 64(2008) 707-720.
- [25] S. Lozano-Perez, *Micron* 39(2008) 320-328.
- [26] F. De La Peña, M.H. Berger, J.F. Hochepped, F. Dynys, O. Stephan, M. Walls, *Ultramicroscopy* 111(2011) 169-176.
- [27] T.L. Daulton, B.J. Little, *Ultramicroscopy* 106(2006) 561-573.
- [28] C. Colliex, T. Manoubi, C. Ortiz, *Phys. Rev. B* 44(1991) 11402-11411.
- [29] B. Stellwag, *Corros. Sci.* 40(1998) 337-370.
- [30] R. Soulas, M. Cheynet, E. Rauch, T. Neisius, L. Legras, C. Domain, Y. Brechet. *J. Mater. Sci.* 48(2013) 2861-2871.
- [31] Y. Han, J. Mei, Q. Peng, E.H. Han, W. Ke, *Corros. Sci.* 112(2016) 625-634.
- [32] B. Langelier, S. Y. Persaud, R. C. Newman, and G. A. Botton. *Acta Mater.* 109(2016) 55-68.
- [33] G. Bertali, F. Scenini, and M. G. Burke. *Corros. Sci.* 100(2015) 474-483.
- [34] D.J. Young, *High temperature oxidation and corrosion of metals (Vol. 1)* (Elsevier, 2008).
- [35] D.S. Morton, S.A. Attanasio, G.A. Young, P.L. Andresen, T.M. Angeliu, *Proc. Corrosion 2011*, NACE International (2001) (paper 01117).

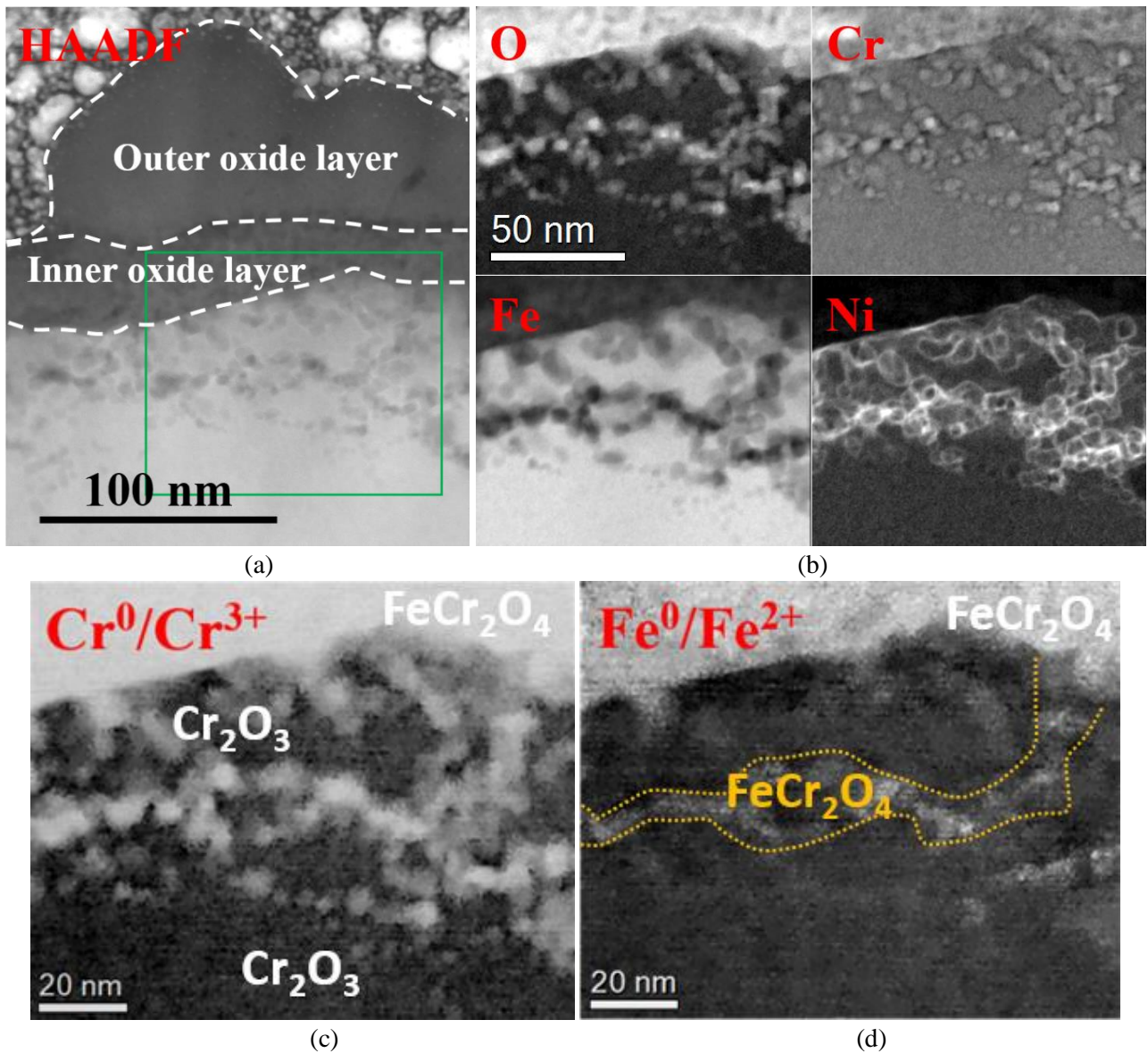
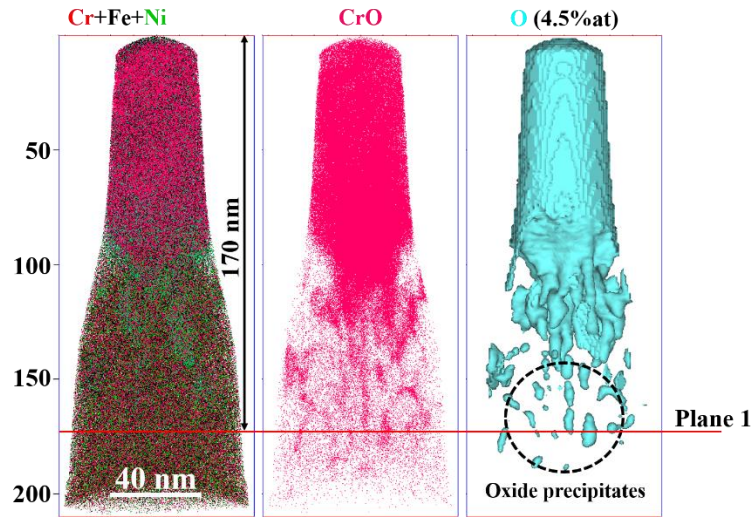
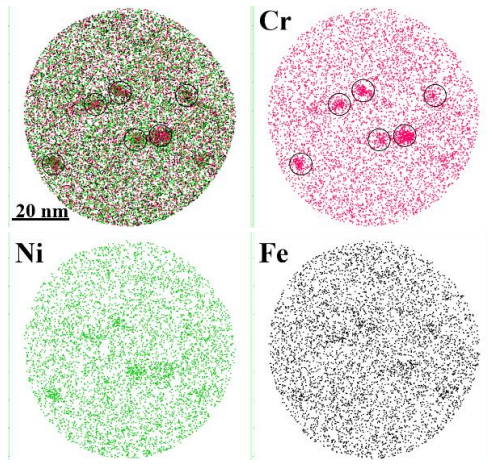


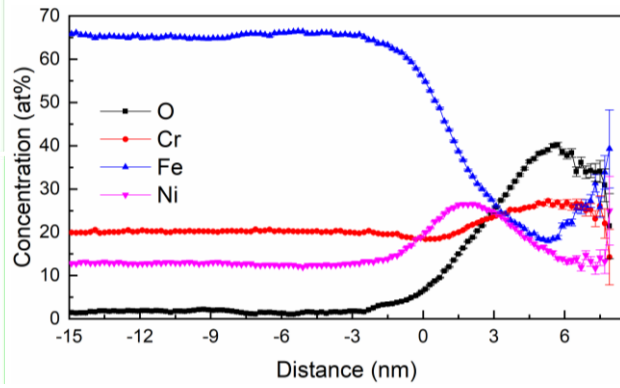
Fig. 1. Surface oxidation of 20% cold-worked 316 SS coupon for 2000h at 340°C (specimen thickness ~30 nm): (a) HAADF image of the cross-section of the surface oxide; (b) EELS signal intensity maps of O, Cr, Fe, and Ni; L3 edge energy-loss maps (brighter means higher energy loss, correlated with a higher oxidation state) showing the different oxidation states of (c) Cr and (d) Fe.



(a)



(b)



(c)

Fig. 2. Surface oxidation of 20% cold-worked 316 SS coupon for 2000h at 340°C: (a) APT data set showing the 3D distribution of Cr/Fe/ Ni (left), CrO (middle), and 4.5 at.% O isosurfaces; (b) a plenary region extracted from the APT data set showing the distribution of oxide precipitates (plane thickness ~8 nm); (c) proxigrams showing the chemical composition across the interfaces marked in (a) (4.5 at.% O, only the discrete oxide precipitates).

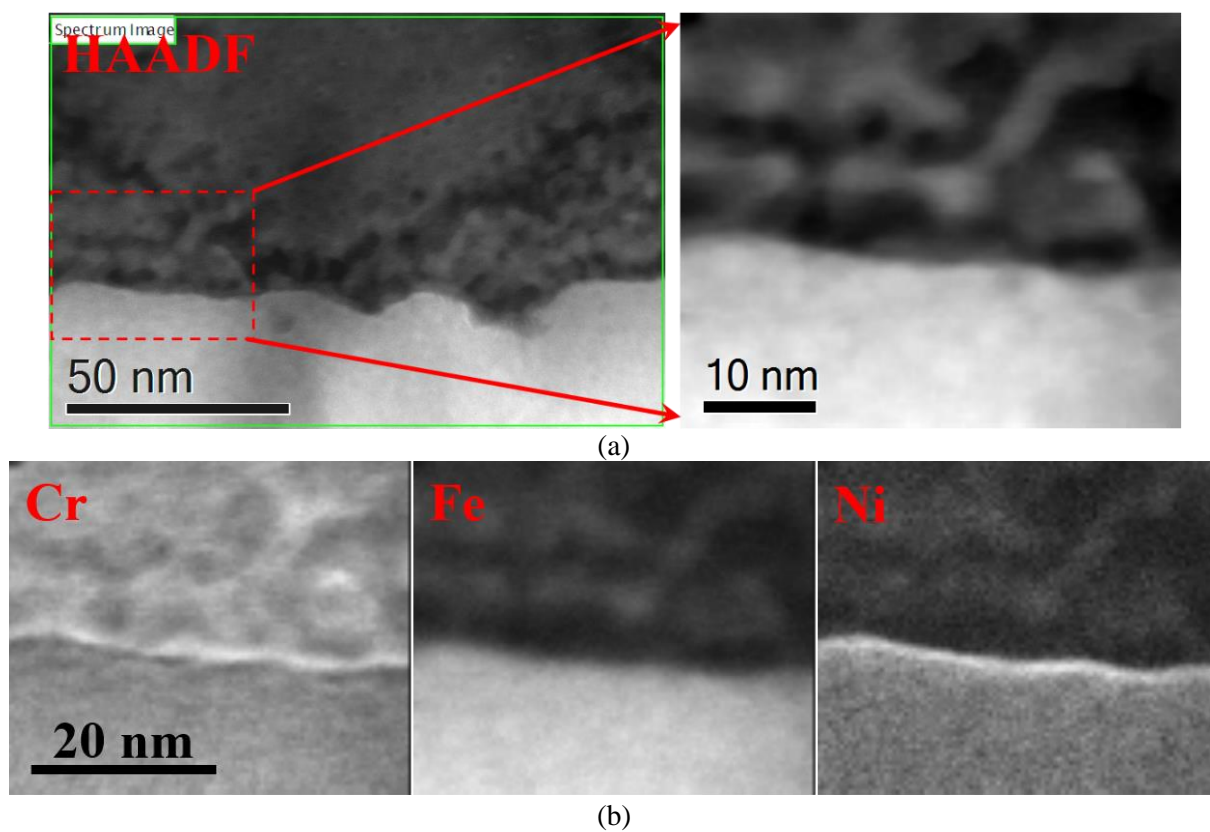
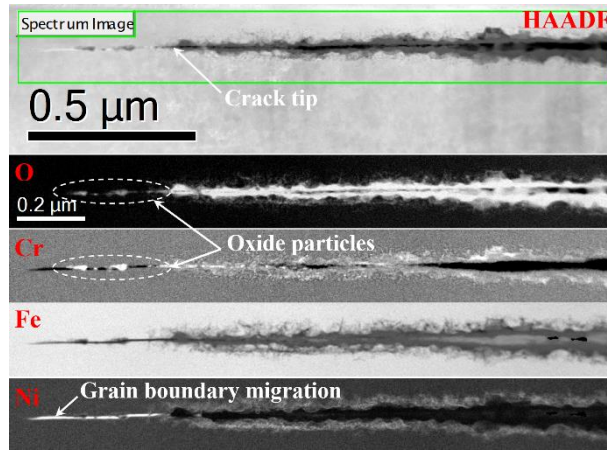
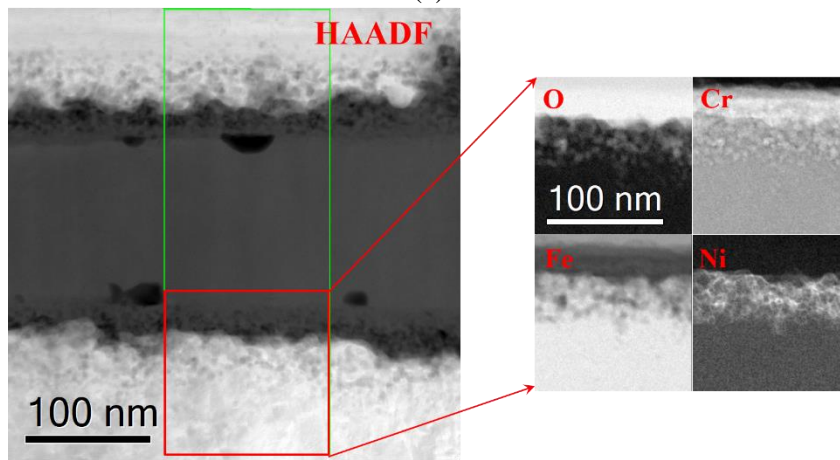


Fig. 3. Surface oxidation of 316 SS coupon without cold-work for 2000h at 340°C: (a) HAADF image of the cross-section of the surface oxide; (b) EELS signal intensity maps of Cr, Fe, and Ni.



(a)



(b)

Fig. 4. IGSCC crack oxidation of 20% cold-worked 316SS at 340°C: (a) intergranular oxidation ahead of the crack tip; (b) intragranular oxidation along the crack [4].